Holo-VQVAE: VQ-VAE for phase-only holograms

Joohyun Park KyungHee University Korea, Republic of

james5450@khu.ac.kr

Hyeongyeop Kang KyungHee University Korea, Republic of

siamiz@khu.ac.kr

Abstract

Holography stands at the forefront of visual technology innovation, offering immersive, three-dimensional visualizations through the manipulation of light wave amplitude and phase. Contemporary research in hologram generation has predominantly focused on image-to-hologram conversion, producing holograms from existing images. These approaches, while effective, inherently limit the scope of innovation and creativity in hologram generation. In response to this limitation, we present Holo-VOVAE, a novel generative framework tailored for phase-only holograms (POHs). Holo-VQVAE leverages the architecture of Vector Quantized Variational AutoEncoders, enabling it to learn the complex distributions of POHs. Furthermore, it integrates the Angular Spectrum Method into the training process, facilitating learning in the image domain. This framework allows for the generation of unseen, diverse holographic content directly from its intricately learned latent space without requiring pre-existing images. This pioneering work paves the way for groundbreaking applications and methodologies in holographic content creation, opening a new era in the exploration of holographic content.

1. Introduction

Holography is an emerging technology that unveils a realm where the conventional boundaries of image capturing and representation are transcended. Traditional photography is confined to recording the amplitude of light waves, making it lose three-dimensionality and present a two-dimensional portrayal of the world. In contrast, holography is able to encapsulate not just the amplitude, but also the phase values of light waves, thereby preserving the spatial information intrinsic to every scene.

Unfortunately, the pace of evolution in 3D holography is slower than that in 2D images due to the technical complexity, expensive equipment, computational intensity, and material limitations [4, 32, 36]. To overcome this, many researchers begin with simpler forms of holography such

as 2D phase-only holograms (POHs). They conduct experiments and test their hypothesis in the 2D domain to obtain a foundational understanding of light's behavior and the principles of interference and diffraction [19, 26]. The gained understanding serves as a prerequisite for exploring the more complex domain of 3D holography. In a similar context, POHs are actively researched because they simplify the data handling process by keeping the amplitude of the wavefront constant and only considering the phase variants information to encode the information of the scene.

These days, the research topic in the image domain has begun to include generative models for 2D images. Such models have transformative potential in synthesizing realistic and high-quality visuals, augmenting datasets, and enhancing various applications from art to healthcare. However, due to its complexity, only a few attempts have been made to translate this success to the realm of holography. In terms of phase data learning, generative models have to process intricate patterns and dependencies between different phases and phase wraps that can cause abrupt changes and discontinuities in the phase data. Furthermore, developing appropriate metrics and loss functions that consider the unique characteristics of phase information becomes a challenge. These contrast with the simple, pixel-based intensity values commonly encountered in 2D images, making it challenging to train generative models for holography.

Previous research of Liu *et al.* [19] demonstrates that a Variational AutoEncoder(VAE) model trained in the phase domain managed to reconstruct the input POH but failed to generate novel samples. This suggests that conventional learning methods face challenges when the model is trained directly in the phase domain.

In this paper, we introduce Holo-VQVAE, a novel end-to-end generative model architecture for 2D POH generation. Inspired by HoloNet [26], we find that using images as input and computing the reconstruction loss in the image domain allows the model to learn the data distribution and sample novel POHs. Specifically, we apply the Angular Spectrum Method (ASM) on the generated POH to reconstruct an image, which is then compared with the input im-

age to compute the reconstruction loss. Though the results generated using a standard VAE were promising, we find that adopting the discrete latent space of Vector-Quantized Variational Autoencoder(VQ-VAE) [28, 40] can further improve the generation quality. The discrete latent space mitigates the entanglement of the learned features, resulting in high-quality POH generation.

In summary, the contributions of this paper are as follows:

- We introduce Holo-VQVAE, a pioneer end-to-end generative model architecture for POHs.
- We facilitate the training process by integrating ASM propagation, enabling training in the image domain rather than the phase domain, and devised a loss function balancing noise and quality through an experimental ratio of 12 loss to perceptual loss.
- We employ the discrete latent space of VQVAE for training the POH with complex distributions and confirmed through experiments that it shows superior performance compared to using the continuous latent space of a standard VAE.

2. Related works

Holograms are fringe patterns that encapsulate the intricate interplay of light waves reflected from a scene. The hologram itself is a two-dimensional surface that contains information about the intensity and phase distribution of light waves, but the image it produces appears three-dimensional and can be viewed from different angles.

Holograms can be produced through two primary methods: optical generation and computational generation, with the latter referred to as Computer-Generated Holography (CGH). In recent years, CGH has gained increasing prominence over optical methods, primarily due to the stringent environmental conditions and precise control required for the generation of optical holograms.

In the idealized conception of CGH, both amplitude and phase play pivotal roles, collaboratively contributing to the multi-dimensional portrayal of scenes with enhanced depth and perspective. However, due to the technological complexities and the economic considerations of spatial light modulators (SLMs), a substantial corpus of holographic research often focuses on either amplitude-only holograms or POHs [13].

Among these, POHs have gained more research attention. This inclination is attributed to the inherent capacity of POHs to yield reconstructions marked by enhanced brightness and clarity [24, 38]. The process of generating POH is intricately connected to phase retrieval, a technique that focuses on deducing the phase of input data from the magnitude of its Fourier transform [31]. Phase retrieval is a complex, non-linear, and ill-posed problem. There are inherent ambiguities and constraints that make the retrieval of

phase information challenging. For this reason, a plethora of algorithms exist in the realm of phase retrieval, each tailored to address specific aspects of these challenges.

Traditionally, algorithmic approaches have long been studied. They are inherently systematic and are grounded in well-defined mathematical principles. Algorithmic approaches can indeed be primarily classified into iterative and non-iterative algorithms. Iterative algorithms for phase retrieval involve a repetitive process of refinement to achieve an accurate estimation of the phase [2, 8, 10, 12, 25, 48]. On the other hand, non-iterative algorithms are characterized by their ability to provide rapid phase estimations, resulting in significantly reduced computation times [20, 22, 37, 39]. However, they are often hampered by issues related to computational intensity, convergence challenges, sensitivity to noise, and the expertise required for implementation.

Recently, the advent and proliferation of deep learning techniques have indeed instigated notable advancements in the field of POH generation. Deep learning facilitates the rapid generation of high-quality POHs by learning intricate patterns of light wave interactions within vast datasets, leading to phase hologram generation that is not only accurate but also adaptable across diverse scenarios and conditions [23, 26, 29, 41–43, 45, 47, 50, 51].

The recent integration of deep learning in POH generation has seen significant strides, yet the incorporation of generative models has not been as pronounced. Generative models, characterized by their sophisticated latent space representations, offer advanced techniques for data manipulation [16, 34, 35, 44]. The integration of these models into POH generation holds the potential to expand the horizon of possibilities in holography, paving the way for innovative applications and methodologies.

One relevant study is Liu *et al.* [19] that introduces a generative approach for hologram generation named channeled variational encoder. This involves an assumption where the target hologram is modeled as the product of the original hologram and a specific transformation function. While this method circumvents the complexities associated with mapping intricate phase data into a latent space, it inherently reveals a limitation to generating more complex scenes that cannot be derived simply by applying a transformation function. Furthermore, augmenting the model's generative range is intrinsically tied to the availability of a dataset volume. Our model markedly deviates from Liu's paradigm, embodying an enhanced capability to directly synthesize unseen POHs from a learned latent space.

3. Method

The overall pipeline of our model, Holo-VQVAE, is illustrated in Figure 1. It is structured around two principal components: the encoder and the decoder. During the training

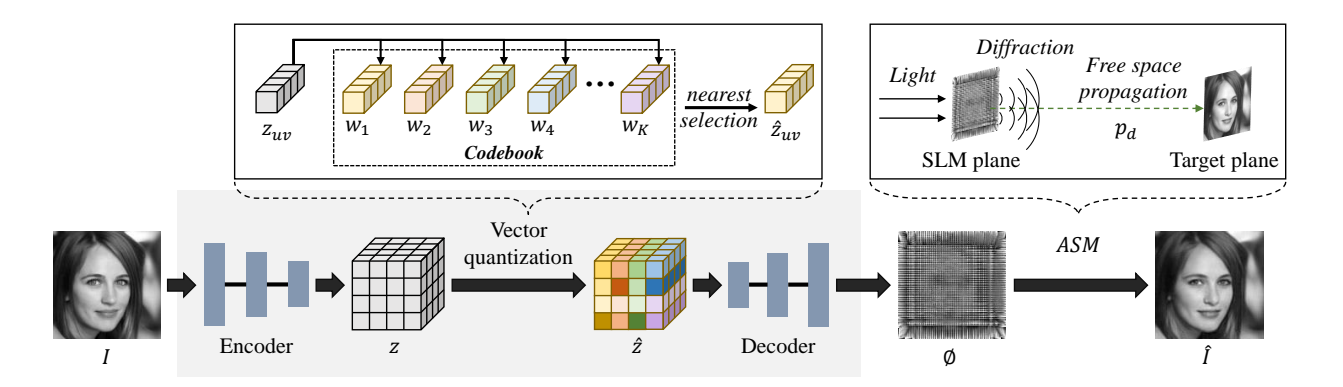


Figure 1. Overall architecture of Holo-VQVAE

phase, the encoder's role is to convert an input 2D image into a corresponding representation within the latent space. Subsequently, the decoder is tasked with the generation of a POH from this latent representation. The objective function regarding reconstruction is computed in the image domain, which aims to minimize the discrepancy between the original input image and the image reconstructed from the POH. The architecture of our model is based on the work by Esser *et al.* [9], which utilizes a discrete latent space [40] to effectively encapsulate the distinctive features of the data. This approach enables a condensed yet richly detailed encoding of the input, ensuring that the essential characteristics are efficiently represented within a compact latent space. The details on model configurations are illustrated in the supplementary material.

3.1. Encoding

The input to the encoder is a 2D image $I \in \mathbb{R}^{N \times N \times C}$, where N denotes the width and height of the image and C specifies its number of channels. The encoding process encompasses the convolution of input features and their subsequent downsampling to yield the latent vector $z \in \mathbb{R}^{n \times n \times H}$, where n denotes its width and height and H specifies its number of channels.

In the design of our Holo-VQVAE architecture, we have determined to use 2D images as the training input, with the output being a POH. This decision is underpinned by two primary considerations.

Firstly, the previous study of Liu *et al.* [19] has reported the significant challenges associated with direct learning from phase data. The inherent complexity and high sensitivity to errors in phase information can severely impede the learning process, often leading to a significant loss in reconstructed results upon minor inaccuracies. By leveraging the image domain, we are able to exploit a wide range of well-established learning strategies, circumventing the complexities inherent to phase data and facilitating a more stable and

effective training process.

Secondly, the scarcity of high-quality POH datasets poses a substantial barrier [49]. Of course, conversion models are available that can turn standard image datasets into POH datasets [26, 51]. However, the quality of the holographic data produced is not always comparable to that of the original images, and the conversion process can be time-consuming. Maintaining the quality of training data is crucial, as any reduction in its quality can negatively impact the performance of the trained model. Hence, we prioritize using datasets in their original form to guarantee the best possible training input for our Holo-VQVAE.

3.2. Vector quantization

The vector quantization process is a crucial step in VQ-VAEs, distinguishing them from standard VAEs by quantizing a continuous latent vector z into a discrete counterpart \hat{z} . This is achieved using a codebook consisting of K representative vectors. For each pixel z_{uv} in the continuous latent space, where $z_{uv} \in \mathbb{R}^{1 \times 1 \times H}$ and $u, v \in n$, we measure its similarity to each codebook vector $w_k \in \mathbb{R}^{1 \times 1 \times H}$, where $k \in K$. The similarity is assessed by computing the squared Euclidean distance. Then, the codebook vector w_k that is most similar to z_{uv} is then chosen as the quantized counterpart $\hat{z}_{uv} \in \mathbb{R}^{1 \times 1 \times H}$. Mathematically, this selection process is defined as follows:

$$\hat{z}_{uv} = \underset{w_k}{\operatorname{argmin}} \|z_{uv} - w_k\|^2$$
 (1)

The quantization process is applied across all pixels, transforming the continuous latent vector z into its discrete equivalent \hat{z} , thereby facilitating the generation of a discrete latent representation of the input data.

3.3. Decoding and reconstruction

During the decoding stage, the quantized vector \hat{z} is processed through a series of convolutional layers and upsampling steps to construct a POH $\phi \in \mathbb{R}^{N \times N \times C}$.

The produced POHs encapsulate phase information in the form of intricate fringe patterns, which do not present a recognizable depiction of the original scene. To convert the patterns back into a visual representation of the scene, a numerical reconstruction process is essential. This typically involves simulating the wavefront propagation, effectively retracing the path of light as captured in the hologram.

For wavefront propagation, our model employs ASM [11, 21], a method recognized for its ability to emulate light wave propagation. The application of ASM to ϕ is defined with the following set of equations, as specified in Equation 2. These equations model the transformation of the wavefront as it propagates from the SLM plane, through free space, experiencing diffraction, and finally arriving at the target plane, where the holographic image is formed:

$$\hat{\phi}_c(p_d) = \iint F\left(e^{i\phi_c}\right) H(f_x, f_y, p_d) e^{i2\pi(f_x x + f_y y)} df_x df_y,$$

$$H(f_x, f_y, p_d) = \begin{cases} e^{i\frac{2\pi}{\lambda_c}} \sqrt{1 - \lambda_c^2 (f_x^2 + f_y^2)} p_d, & \text{if } \sqrt{f_x^2 + f_y^2} < \frac{1}{\lambda_c}, \\ 0 & \text{otherwise} \end{cases}$$
(2)

where p_d denotes the propagation distance, ϕ_c denotes the $c \in C$ channel of ϕ , $\hat{\phi}_c$ denotes the propagated wavefront of ϕ_c at distance p_d , F denotes the Fourier Transform, λ_c denotes the wavelength corresponding to channel $c, x \in N$ and $y \in N$ denote the spatial coordinates, and f_x and f_y denote the spatial frequency components of ϕ_c in the x and y directions. It is important to note that ASM is applied separately to each color channel, as the wavelength λ_c varies for different colors in the light spectrum.

The propagated wavefront $\hat{\phi}$ contains both amplitude and phase information. Here, the phase information does not directly contribute to the perceived image but rather to the way light interferes to form that image. In contrast, the amplitude pattern is what needs to be visualized to represent the reconstructed image from a hologram. Therefore, it is essential to extract the amplitude patterns of $\hat{\phi}$. The amplitude extraction is defined by the following equations:

$$\hat{I} = s \cdot |\hat{\phi}| \tag{3}$$

where \hat{I} denotes the reconstructed image and s denotes a hyperparameter representing a variable for considering the gap between the output values of the wave propagation operator (ASM) and the desired target [26].

3.4. Objective function

The Holo-VQVAE model's objective function is articulated through a tripartite formulation, encompassing reconstruction loss (L_{recon}), codebook loss ($L_{codebook}$), and commitment loss (L_{commit}), each serving a distinct purpose in the training process.

The reconstruction loss, L_{recon} , quantifies the fidelity of the reconstructed output \hat{I} relative to the original input I. It comprises of an l2 loss and the perceptual loss L_{per} [14] between the images. The perceptual loss works by feeding both the input and the reconstructed image into a pretrained VGG16 network to compare their feature maps extracted at designated layers. The layers for feature extraction are determined by the target features for comparison. Early layers capture low-level features like edges and blobs, whereas deeper layers reveal high-level semantic features [27]. Our model employs features extracted from ReLU 2-2 and ReLU 4-3 for a comprehensive comparison that encompasses both the low-level and high-level features.

Our reconstruction loss is computed as a weighted sum of the l2 norm and the perceptual loss L_{per} [14], as delineated in Equation 4:

$$L_{recon} = \alpha \cdot ||I - \hat{I}||_2^2 + \beta \cdot L_{per}(I, \hat{I})$$
 (4)

where α and β are the respective weights assigned to the l2 norm and perceptual loss components. We discover that incorporating the L_{per} can mitigate the noise artifacts within the generated POHs, a phenomenon further explained upon in subsection 4.1

The codebook loss, $L_{codebook}$, and the commitment loss, L_{commit} , are integral to the VQ-VAE architectures, ensuring the encoder's outputs maintain a coherent relationship with the codebook vectors. The $L_{codebook}$, as specified in Equation 5, updates the codebook vectors to better approximate the encoder's outputs, thereby encapsulating the data distribution more effectively:

$$L_{codebook} = ||sg[z] - \hat{z}||_2^2 \tag{5}$$

where sg denotes the stop-gradient operation that prevents gradient information from flowing back.

The L_{commit} optimizes the encoder to produce latent vectors that closely align with the codebook vectors, as expressed in Equation 6. This loss component restricts the latent space from becoming excessively expansive and ensures its conformity to a certain embedding:

$$L_{commit} = ||z - sg[\hat{z}]||_2^2 \tag{6}$$

The aggregate objective function of Holo-VQVAE, therefore, is the summation of these individual losses, formalized in Equation 7:

$$L_{total} = L_{recon} + L_{codebook} + L_{commit} \tag{7}$$

3.5. Sampling

For a standard VAE, the latent space is designed to follow a continuous Gaussian distribution, which allows for easy sampling. The generation of novel data can be achieved by sampling a vector from the Gaussian distribution, which is then passed to the decoder for reconstruction.

In contrast, VQ-VAEs exploit a discrete latent space where the input to the decoder is represented by a combination of the codebook vectors. Since it is not straightforward to sample from this space, an additional model is trained to sample appropriate sequences of the codebook vectors for the generation of new samples.

We select PixelSnail [7] as the sampling model for Holo-VQVAE. Other models including diffusion-based [30] and transformer-based [9] methods may provide better sampling results, but we leave that to future works. The details on PixelSnail configurations are illustrated in the supplementary material.

4. Experiments

We evaluate our model using datasets of MNIST [18], Fashion-MNIST [46] and CelebA-HQ [15] datasets. The images are resized to 128×128 for CelebA-HQ, and 64×64 for MNIST and Fashion-MNIST. The propagation distance p_d is set to 15 mm and 21.5 mm for images with 64×64 and 128×128 resolutions, respectively. The hyperparameter variable s used in the amplitude extraction is set to 0.95, following the implementation of Holonet [26]. The optimizer is set to ADAM with a learning rate of 0.0002, and the model was trained on each dataset for 100 epochs on a single NVIDIA Geforce RTX 3090 GPU. Further details can be found in the supplementary materials.

The performance of our model was assessed using Peak Signal-to-Noise Ratio (PSNR), Structural Similarity Index Measure (SSIM), and Fréchet Inception Distance (FID) as metrics.

PSNR calculates the ratio between the maximum possible power of a signal (in this paper, an image) and the power of distorting noise that affects the quality of its representation. A higher PSNR generally indicates better reconstruction quality.

SSIM is used to measure the similarity between two images by considering changes in structural information, luminance, and contrast. SSIM values range between -1 and 1, where 1 indicates perfect similarity.

FID measures the distribution similarity between the generated images and the real images. A lower FID score indicates a greater similarity, with a score of 0 being the exact match.

4.1. Reconstruction loss

In image synthesis, generative models typically incorporate either l2 loss or perceptual loss to enhance reconstruction quality. The implementation of l2 loss aims at minimizing pixel-level discrepancies between the generated and target images, thereby achieving high fidelity in pixel-value correspondence. Conversely, perceptual loss [14, 33], aims at

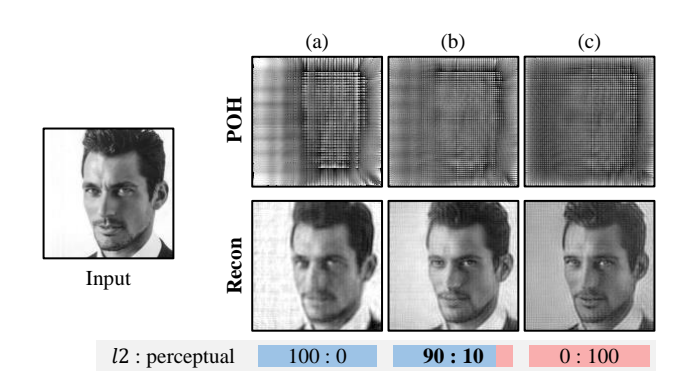


Figure 2. An illustration of example POH reconstructions utilizing diverse loss functions: (a) employing a model trained solely on l2 loss; (b) employing a model trained on a loss function that integrates l2 loss with perceptual loss in a 9:1 ratio; (c) employing a model trained solely on perceptual loss. The examples present only a single channel (green) of the input for better noise visualization.

l2: perceptual	Metric	MNIST	Fashion-MNIST	CelebA-HQ
100:0	PSNR	33.53	32.24	26.91
100.0	SSIM	0.76	0.82	0.78
90:10	PSNR	31.86	30.38	24.70
90:10	SSIM	0.71	0.79	0.73
0:100	PSNR	23.09	23.14	17.74
0.100	SSIM	0.41	0.66	0.62

Table 1. The average scores of PSNR and SSIM were assessed for the Holo-VQVAE, trained with diverse *l2*: perceptual ratios, using test datasets including MNIST, Fashion-MNIST, and CelebA-HQ datasets.

enhancing the perceptual similarity between images, aligning more congruently with human visual processing mechanisms

Upon applying the perceptual loss for POH synthesis, we observed that it can also suppress the generation of noise [3, 5, 6] in the reconstructed images. When the POH was generated from the model trained only on the l2 loss, the reconstructed image shows noticeable noise, as shown in Figure 2 (a). Conversely, when the POH was generated from the model trained only on the perceptual loss, the reconstructed image shows pixel value difference compared to the input image, as shown in Figure 2 (c). Here, we speculate that perceptual loss may contribute to regulating and smoothing the noise in the generation of POH.

The sole use of the perceptual loss, however, results in a noticeable drop in the average PSNR and SSIM scores on the reconstruction as shown in Table 1. In light of these insights, we combined l2 loss with the perceptual loss in a 9:1 ratio, as demonstrated in Figure 2 (b). This combination was empirically engineered to harmonize the PSNR and SSIM metrics, thereby optimizing the reconstruction quality.

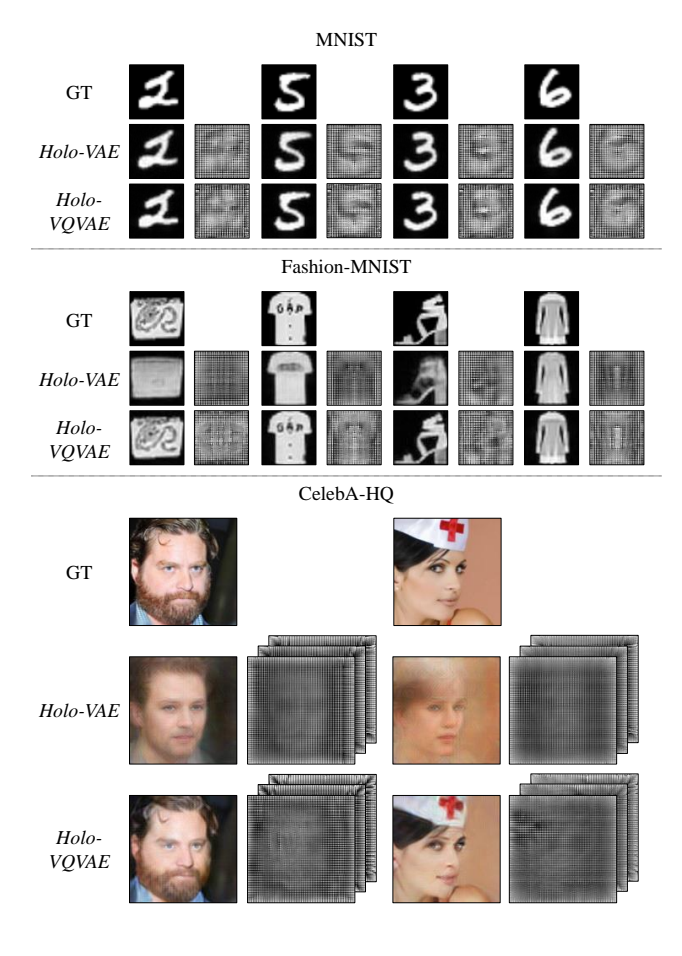


Figure 3. POHs and their reconstructions, generated with *Holo-VAE* and *Holo-VQVAE*, using ground truth (GT) images from MNIST, Fashion-MNIST, and CelebA-HQ datasets.

Model	Metric	MNIST	Fashion-MNIST	CelebA-HQ
Holo-VAE	PSNR	23.89	21.75	17.63
HOIO-VAE	SSIM	0.65	0.60	0.46
Holo-VOVAE	PSNR	31.86	30.38	24.70
11010-VQVAL	SSIM	0.71	0.79	0.73

Table 2. PSNR and SSIM scores on the reconstructed validation set images for *Holo-VAE* and *Holo-VQVAE*.

4.2. Evaluation on reconstruction and sampling

We conducted comparative evaluations from both reconstruction and sampling perspectives to validate whether our architecture design successfully serves our purpose. Since there are no existing studies with networks that have successfully achieved our goal of generating POHs, the evaluation focused on two internally developed approaches: *Holo-VAE* and *Holo-VOVAE*.

Holo-VAE refers to our initial architecture, employing a standard VAE architecture instead of a VQ-VAE. The objective function of this architecture comprises a reconstruc-

tion loss and a KL-divergence loss, which collectively ensure that the latent space conforms to a Gaussian distribution. Our choice to begin with the VAE was influenced by its straightforward nature and the existing foundation of research demonstrating its potential in similar applications. We hypothesized that employing a VAE, with a carefully devised reconstruction loss L_{recon} , would yield high-fidelity POHs, both in reconstruction and sampling tasks. Holo-VQVAE refers to our architecture described in this paper.

The result of reconstructions is shown in Figure 3. While *Holo-VAE* appears to capture essential features of the ground truth images and generate plausible outputs, it fails to capture high-level details and results in blurred images. We speculate that this could be attributed to VAE's assumption that the latent space comprises Gaussian distributions. High-level details often correspond to less probable regions in a Gaussian distribution, and the VAE's regularization (KL-divergence loss) may inadvertently smooth out these details to fit the Gaussian model. This problem of course can be mitigated by reducing the weight of the KL-divergence loss. However, this inevitably compromises the sampling ability [1].

Conversely, the *Holo-VQVAE* demonstrates a notable proficiency in generating results that are both clearer and more adept at restoring high-level details. We speculate that this enhanced performance can be attributed to VQ-VAE's utilization of discrete latent space. The discrete representation allows VQ-VAE to handle complex distributions like POH data and preserve distinct features that might be averaged out or lost in the continuous latent space of a VAE [40].

The quantitative evaluation of reconstruction tasks, as indicated by the PSNR and SSIM scores, is detailed in Table 2. These results demonstrate that *Holo-VQVAE* generally outperforms *Holo-VAE* in terms of reconstruction quality. Particularly, the enhancement in scores is more pronounced as the dataset complexity escalates from MNIST to CelebA-HQ.

Subsequently, the result of the sampling task is shown in Figure 4. This task involves generating new, unseen POHs that are representative of the training dataset, thereby demonstrating the model's generative capabilities.

Similar to the reconstruction task, *Holo-VAE* often resulted in images with a loss of high-level detail and a blurred appearance. In contrast, the *Holo-VQVAE* produced images that were clear and rich in high-level details. The effectiveness of each model in this task is quantitatively assessed using the FID scores, which measure the similarity between a set of 100 generated samples and a random selection of 100 images from the validation set. As indicated in Table 3, the *Holo-VQVAE* demonstrates superior performance in terms of FID scores, with the improvement being more pronounced as the dataset transitions from the less

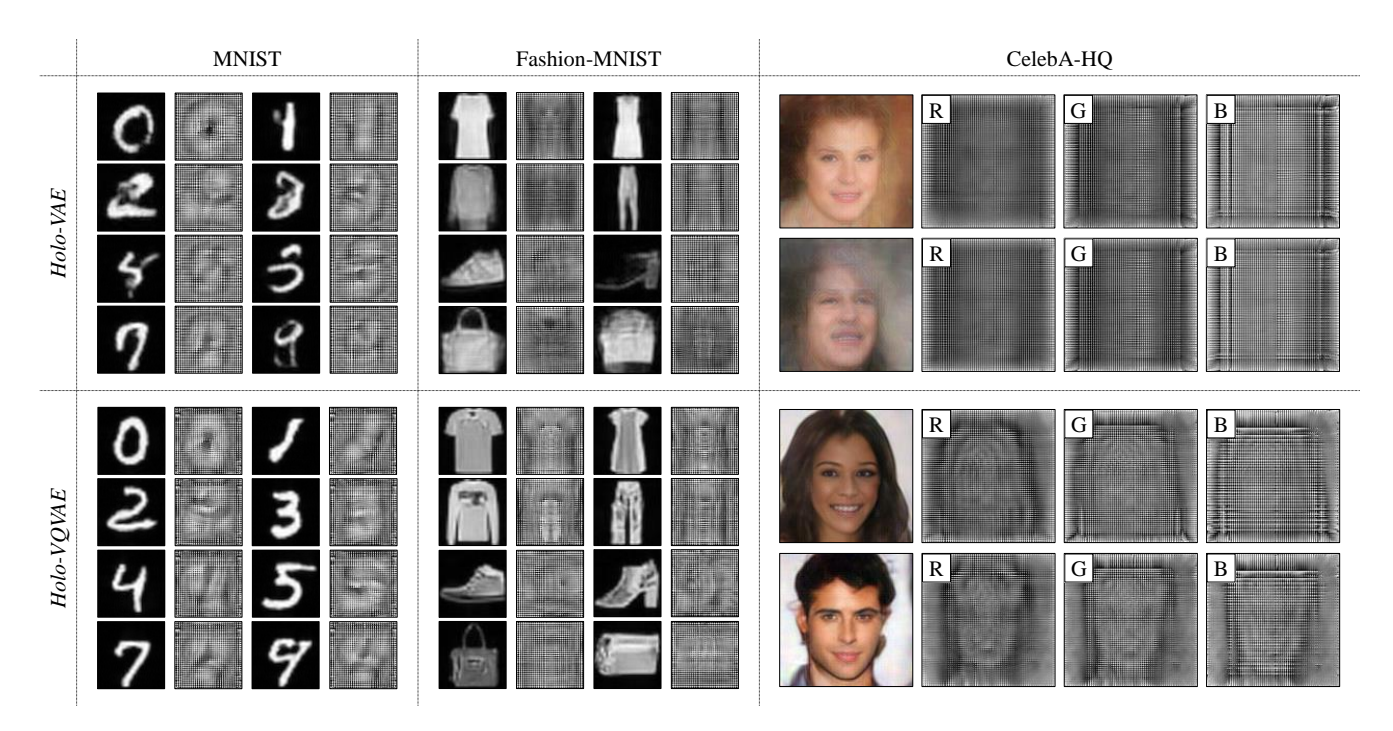


Figure 4. Representative POH samples and their reconstructions of *Holo-VAE* and *Holo-VQVAE* trained on MNIST, Fashion-MNIST, and Celeba-HQ datasets. The R, G, and B placed on the top-left refer to the RGB channels of the sample POH, respectively.

Model	Metric	MNIST	Fashion-MNIST	CelebA-HQ	
Holo-VAE	FID	134.7	209.1	173.9	
Holo-VQVAE	TID	102.1	162.7	134.1	

Table 3. FID scores on the reconstructions of sample POHs for *Holo-VAE* and *Holo-VQVAE*.

complex MNIST to the more intricate CelebA-HQ. More samples from *Holo-VQVAE* can be found in the supplementary material.

It is important to note that the FID scores for our models are relatively high when compared to those of recent image generation models. This discrepancy can be attributed to the inherent challenges in generating high-fidelity POHs, a task that is fundamentally more complex and nuanced than typical image generation. The presence of noise, a factor we aimed to mitigate as discussed in subsection 4.1, also contributes to these higher scores. We anticipate that ongoing advancements and refinements in our approach will lead to improved FID scores in the future.

5. Limitations and future work

In addressing the limitations and future directions of our research, three key aspects warrant attention.

Firstly, the resolution of the generated POHs presents a significant challenge. Our model currently supports resolutions up to 256×256 pixels, as demonstrated in Figure 5. However, for practical applications in holography,

notably higher resolutions are required. This need stems from the specifications of holographic displays, which typically feature pixel sizes ranging from 3 to 60 μm [17]. Consequently, an image reconstructed at our model's highest resolution of 256×256 translates to a physical size of merely about 1.536~cm in both width and height. This size is considerably smaller than what is needed for effective visualization in real-world scenarios, such as in holographic displays or augmented reality devices. Addressing this limitation involves not only scaling up the resolution but also ensuring that the increase in resolution does not compromise the quality of the holographic reconstruction.

Secondly, our model's current design generates POHs optimized for a fixed propagation distance p_d . While this approach ensures quality reconstructions at this specific distance, it limits the hologram's effectiveness for viewers positioned at varying distances. Therefore, it is crucial to develop methods that allow for variable propagation distances in the training process. Such an advancement would enable the generation of POHs that maintain high-quality reconstructions across a range of distances, significantly enhancing the versatility and applicability of our holographic models in diverse real-world settings.

Lastly, it is noteworthy that our study did not incorporate experimental validation using real optical devices for assessing the reconstruction quality. This decision was grounded as our primary aim was to assess the algorithmic effectiveness of the learning strategies for high-fidelity

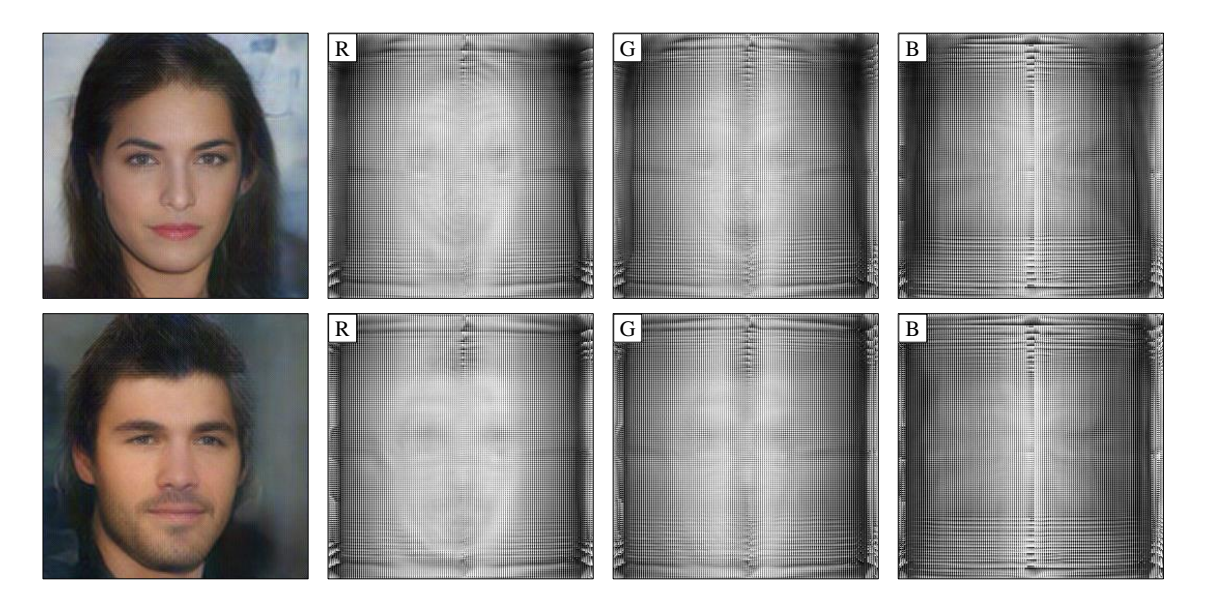


Figure 5. Representative POH samples and their reconstructions of Holo-VQVAE trained on CelebA-HQ of resolution 256×256 . The R, G, and B placed on the top-left refer to the RGB channels of the sample POH, respectively.

POH generation. Advances in computational holography allow for accurate predictions and assessments of hologram quality through simulations, aligning with current research trends where computational validation often precedes resource-intensive optical testing. However, we acknowledge that future work involving the practical application of these models would benefit from experimental validation using optical setups, to fully ascertain their effectiveness in real-world holographic display scenarios. Therefore, future work will benefit from optical validation to bridge the gap between theoretical development and practical application.

6. Conclusion

Recent image generation methods leveraging generative models have unlocked a plethora of creative possibilities, ranging from seamless image interpolation to intricate text-driven modifications. The cornerstone of these advancements lies in the effective utilization of latent spaces which distilled the crucial features of target data.

Despite these advancements in image generation, the field of holography, particularly a generative model for hologram generation, has yet to fully embrace the potential of latent spaces. This omission has constrained the holography domain from accessing the advanced capabilities inherent in generative models, thereby limiting the scope of innovation and creativity in hologram generation.

To bridge this gap, we present Holo-VQVAE, a novel framework designed to integrate the generative models into the domain of hologram generation. As a pioneering effort, Holo-VQVAE marks a significant stride towards enriching the holography field with the advanced functionalities of generative models. We anticipate that this integration will catalyze a wave of novel methodologies, expanding the horizons of holographic technology. Therefore, the potential of Holo-VQVAE extends beyond current applications, promising to unlock new realms of exploration and innovation in the creation and manipulation of holographic content.

References

- [1] Andrea Asperti and Matteo Trentin. Balancing reconstruction error and kullback-leibler divergence in variational autoencoders. *IEEE Access*, 8:199440–199448, 2020. 6
- [2] Jörgen Bengtsson. Kinoform design with an optimalrotation-angle method. *Applied optics*, 33(29):6879–6884, 1994. 2
- [3] Vittorio Bianco, Pasquale Memmolo, Marco Leo, Silvio Montresor, Cosimo Distante, Melania Paturzo, Pascal Picart, Bahram Javidi, and Pietro Ferraro. Strategies for reducing speckle noise in digital holography. *Light: Science & Appli*cations, 7(1):48, 2018. 5
- [4] Pierre-Alexandre Blanche. Holography, and the future of 3d display. *Light: Advanced Manufacturing*, 2(4):446–459, 2021.
- [5] Chenliang Chang, Jun Xia, Lei Yang, Wei Lei, Zhiming Yang, and Jianhong Chen. Speckle-suppressed phase-only holographic three-dimensional display based on doubleconstraint gerchberg–saxton algorithm. *Applied optics*, 54 (23):6994–7001, 2015. 5
- [6] Chenliang Chang, Yijun Qi, Jun Wu, Jun Xia, and Shouping Nie. Speckle reduced lensless holographic projection from

- phase-only computer-generated hologram. *Optics Express*, 25(6):6568–6580, 2017. 5
- [7] Xi Chen, Nikhil Mishra, Mostafa Rohaninejad, and Pieter Abbeel. Pixelsnail: An improved autoregressive generative model. In *International Conference on Machine Learning*, pages 864–872. PMLR, 2018. 5
- [8] Thomas Dresel, Mathias Beyerlein, and Johannes Schwider. Design of computer-generated beam-shaping holograms by iterative finite-element mesh adaption. *Applied Optics*, 35 (35):6865–6874, 1996. 2
- [9] Patrick Esser, Robin Rombach, and Bjorn Ommer. Taming transformers for high-resolution image synthesis. In *Proceedings of the IEEE/CVF conference on computer vision and pattern recognition*, pages 12873–12883, 2021. 3, 5
- [10] Ralph W Gerchberg. A practical algorithm for the determination of plane from image and diffraction pictures. *Optik*, 35(2):237–246, 1972.
- [11] Joseph W Goodman. Introduction to Fourier optics. Roberts and Company publishers, 2005. 4
- [12] Toufic G Jabbour and Stephen M Kuebler. Vectorial beam shaping. Optics Express, 16(10):7203–7213, 2008. 2
- [13] Shuming Jiao, Zhi Jin, Chenliang Chang, Changyuan Zhou, Wenbin Zou, and Xia Li. Compression of phase-only holograms with jpeg standard and deep learning. *Applied Sciences*, 8(8):1258, 2018. 2
- [14] Justin Johnson, Alexandre Alahi, and Li Fei-Fei. Perceptual losses for real-time style transfer and super-resolution. In Computer Vision–ECCV 2016: 14th European Conference, Amsterdam, The Netherlands, October 11-14, 2016, Proceedings, Part II 14, pages 694–711. Springer, 2016. 4, 5
- [15] Tero Karras, Timo Aila, Samuli Laine, and Jaakko Lehtinen. Progressive growing of gans for improved quality, stability, and variation. arXiv preprint arXiv:1710.10196, 2017. 5
- [16] Seung Wook Kim, Karsten Kreis, Daiqing Li, Antonio Torralba, and Sanja Fidler. Polymorphic-gan: Generating aligned samples across multiple domains with learned morph maps. In *Proceedings of the IEEE/CVF Conference on Computer Vision and Pattern Recognition*, pages 10630–10640, 2022. 2
- [17] Hyunsuk Ko and Hui Yong Kim. Deep learning-based compression for phase-only hologram. *IEEE Access*, 9:79735–79751, 2021. 7
- [18] Yann LeCun, Corinna Cortes, Chris Burges, et al. Mnist handwritten digit database, 2010. 5
- [19] Sheng-Chi Liu and Daping Chu. Deep learning for hologram generation. *Optics Express*, 29(17):27373–27395, 2021. 1, 2, 3
- [20] Adoph W Lohmann and DP Paris. Binary fraunhofer holograms, generated by computer. *Applied optics*, 6(10):1739–1748, 1967.
- [21] Kyoji Matsushima and Tomoyoshi Shimobaba. Band-limited angular spectrum method for numerical simulation of free-space propagation in far and near fields. *Optics express*, 17 (22):19662–19673, 2009. 4
- [22] Omel Mendoza-Yero, Gladys Mínguez-Vega, and Jesús Lancis. Encoding complex fields by using a phase-only optical element. *Optics letters*, 39(7):1740–1743, 2014.

- [23] Inkyu Moon, Keyvan Jaferzadeh, Youhyun Kim, and Bahram Javidi. Noise-free quantitative phase imaging in gabor holography with conditional generative adversarial network. *Optics Express*, 28(18):26284–26301, 2020. 2
- [24] Hui Pang, Jiazhou Wang, Man Zhang, Axiu Cao, Lifang Shi, and Qiling Deng. Non-iterative phase-only fourier hologram generation with high image quality. *Optics Express*, 25(13): 14323–14333, 2017.
- [25] Yifan Peng, Xiong Dun, Qilin Sun, and Wolfgang Heidrich. Mix-and-match holography. ACM Trans. Graph., 36(6):191– 1, 2017. 2
- [26] Yifan Peng, Suyeon Choi, Nitish Padmanaban, and Gordon Wetzstein. Neural holography with camera-in-the-loop training. ACM Transactions on Graphics (TOG), 39(6):1–14, 2020. 1, 2, 3, 4, 5
- [27] Mohammad Saeed Rad, Behzad Bozorgtabar, Urs-Viktor Marti, Max Basler, Hazim Kemal Ekenel, and Jean-Philippe Thiran. Srobb: Targeted perceptual loss for single image super-resolution. In Proceedings of the IEEE/CVF international conference on computer vision, pages 2710–2719, 2019. 4
- [28] Ali Razavi, Aaron Van den Oord, and Oriol Vinyals. Generating diverse high-fidelity images with vq-vae-2. Advances in neural information processing systems, 32, 2019.
- [29] Yair Rivenson, Yibo Zhang, Harun Günaydın, Da Teng, and Aydogan Ozcan. Phase recovery and holographic image reconstruction using deep learning in neural networks. *Light: Science & Applications*, 7(2):17141–17141, 2018. 2
- [30] Robin Rombach, Andreas Blattmann, Dominik Lorenz, Patrick Esser, and Björn Ommer. High-resolution image synthesis with latent diffusion models. In *Proceedings of* the IEEE/CVF conference on computer vision and pattern recognition, pages 10684–10695, 2022. 5
- [31] Yoav Shechtman, Yonina C Eldar, Oren Cohen, Henry Nicholas Chapman, Jianwei Miao, and Mordechai Segev. Phase retrieval with application to optical imaging: a contemporary overview. *IEEE signal processing magazine*, 32(3):87–109, 2015. 2
- [32] Tomoyoshi Shimobaba, Takashi Kakue, and Tomoyoshi Ito. Review of fast algorithms and hardware implementations on computer holography. *IEEE Transactions on Industrial Informatics*, 12(4):1611–1622, 2015. 1
- [33] Shane D Sims. Frequency domain-based perceptual loss for super resolution. In 2020 IEEE 30th International Workshop on Machine Learning for Signal Processing (MLSP), pages 1–6. IEEE, 2020. 5
- [34] Jaskirat Singh, Stephen Gould, and Liang Zheng. High-fidelity guided image synthesis with latent diffusion models. In 2023 IEEE/CVF Conference on Computer Vision and Pattern Recognition (CVPR), pages 5997–6006. IEEE, 2023. 2
- [35] Ivan Skorokhodov, Sergey Tulyakov, and Mohamed Elhoseiny. Stylegan-v: A continuous video generator with the price, image quality and perks of stylegan2. In *Proceedings of the IEEE/CVF Conference on Computer Vision and Pattern Recognition*, pages 3626–3636, 2022. 2
- [36] Fernando Torres-Leal, Hugo A Moreno-Rodriguez, Juan P Rubio-Perez, Raul I Hernandez-Aranda, Carmelo Rosales-Guzmán, and Benjamin Perez-Garcia. Low-cost printed

- holography for the generation of structured light. *Applied Optics*, 62(26):7104–7110, 2023.
- [37] PWM Tsang, Y-T Chow, and T-C Poon. Generation of phaseonly fresnel hologram based on down-sampling. *Optics express*, 22(21):25208–25214, 2014. 2
- [38] PWM Tsang, J-P Liu, H Lam, and T-C Poon. Optimal sampled phase-only hologram (ospoh). *Optics Express*, 29(16): 25488–25498, 2021.
- [39] Peter Wai Ming Tsang and T-C Poon. Novel method for converting digital fresnel hologram to phase-only hologram based on bidirectional error diffusion. *Optics express*, 21 (20):23680–23686, 2013. 2
- [40] Aaron Van Den Oord, Oriol Vinyals, et al. Neural discrete representation learning. Advances in neural information processing systems, 30, 2017. 2, 3, 6
- [41] Fei Wang, Yaoming Bian, Haichao Wang, Meng Lyu, Giancarlo Pedrini, Wolfgang Osten, George Barbastathis, and Guohai Situ. Phase imaging with an untrained neural network. *Light: Science & Applications*, 9(1):77, 2020. 2
- [42] Hao Wang, Meng Lyu, and Guohai Situ. eholonet: a learning-based end-to-end approach for in-line digital holographic reconstruction. *Optics express*, 26(18):22603–22614, 2018.
- [43] Kaiqiang Wang, Jiazhen Dou, Qian Kemao, Jianglei Di, and Jianlin Zhao. Y-net: a one-to-two deep learning framework for digital holographic reconstruction. *Optics Letters*, 44 (19):4765–4768, 2019. 2
- [44] Tengfei Wang, Yong Zhang, Yanbo Fan, Jue Wang, and Qifeng Chen. High-fidelity gan inversion for image attribute editing. In *Proceedings of the IEEE/CVF Conference on Computer Vision and Pattern Recognition*, pages 11379– 11388, 2022. 2
- [45] Jiachen Wu, Kexuan Liu, Xiaomeng Sui, and Liangcai Cao. High-speed computer-generated holography using an autoencoder-based deep neural network. *Optics Letters*, 46 (12):2908–2911, 2021. 2
- [46] Han Xiao, Kashif Rasul, and Roland Vollgraf. Fashion-mnist: a novel image dataset for benchmarking machine learning algorithms. arXiv preprint arXiv:1708.07747, 2017.
- [47] Da Yin, Zhongzheng Gu, Yanran Zhang, Fengyan Gu, Shouping Nie, Jun Ma, and Caojin Yuan. Digital holographic reconstruction based on deep learning framework with unpaired data. *IEEE Photonics Journal*, 12(2):1–12, 2019.
- [48] Nobukazu Yoshikawa, Masahide Itoh, and T Yatagai. Quantized phase optimization of two-dimensional fourier kinoforms by a genetic algorithm. *Optics Letters*, 20(7):752–754, 1995.
- [49] Tianjiao Zeng, Yanmin Zhu, and Edmund Y Lam. Deep learning for digital holography: a review. *Optics Express*, 29(24):40572–40593, 2021. 3
- [50] Gong Zhang, Tian Guan, Zhiyuan Shen, Xiangnan Wang, Tao Hu, Delai Wang, Yonghong He, and Ni Xie. Fast phase retrieval in off-axis digital holographic microscopy through deep learning. *Optics express*, 26(15):19388–19405, 2018. 2
- [51] Yuhe Zhang, Mike Andreas Noack, Patrik Vagovic, Kamel Fezzaa, Francisco Garcia-Moreno, Tobias Ritschel, and

Pablo Villanueva-Perez. Phasegan: a deep-learning phase-retrieval approach for unpaired datasets. *Optics express*, 29 (13):19593–19604, 2021. 2, 3

Holo-VQVAE: VQ-VAE for phase-only holograms

Supplementary material

Joohyun Park KyungHee University Korea, Republic of

Hyeongyeop Kang KyungHee University Korea, Republic of

james5450@khu.ac.kr

siamiz@khu.ac.kr

1. Implementation details

1.1. Holo-VQVAE

The architecture of Holo-VQVAE is built upon the work of Esser *et al.* [?]. Figure 1 illustrates the detailed pipeline of our model, where I denotes the input image, N denotes the width and height of I, C denotes the number of channels of I, z denotes the latent vector, n denotes the width and height of z, H specifies the number of channels of z, \hat{z} denotes the vector quantized latent vector, ϕ denotes the generated phase-only hologram (POH), and \hat{I} denotes the reconstructed image. The hyperparameter m determines the compression rate for the latent vector, where higher values of m indicate greater compression. A Hardtanh activation function is employed at the end of the decoder to ensure that the values of the generated POH are in the range of $-\pi$ to π .

The specific model configurations for each resolution are shown in Table 1, where K denotes the number of representative vectors in the codebook, p_d denotes the propagation distance, s denotes the variable used in the amplitude extraction, and λ denotes the wavelength. To maintain a consistent latent vector size of 16×16 across various input resolutions, m is set to 3 for inputs with a resolution of 64×64 , 4 for 128×128 , and 5 for 256×256 . The wavelength value λ leveraged for the Angular Spectrum Method (ASM) is set to 638 nm, 520 nm, and 450 nm for red, green, and blue channels, respectively. The optimizer for training is set to ADAM with a learning rate of 0.0002, and the model was trained on each dataset for 100 epochs on a single NVIDIA Geforce RTX 3090 GPU.

Resolution	Batch size	m	H	K	p_d	s	λ
64×64	50	2			15 mm		
128×128	20	3	256	512	21.5 mm	0.95	(638 <i>nm</i> , 520 <i>nm</i> , 450 <i>nm</i>)
256×256	5	4			25 mm		

Table 1. Holo-VQVAE configurations for various input resolutions.

1.2. PixelSnail

Our implementation of PixelSnail [?] is built upon the work of Razavi et al. [?]. The model configurations are listed on Table 2, which maintains consistency across all experiments of various resolutions. The input size of the model is fixed to 16×16 , aligning with the size of Holo-VQVAE's latent vectors. The model is composed of a series of layers that include both residual and attention layers. Specifically, for every four residual layers, one attention layer follows behind. As our implementation comprises 20 layers in total, it incorporates four attention layers. Each attention layer is designed with 8 attention heads, which facilitates the model's ability to focus on different parts of the input simultaneously. This dropout is implemented at a rate of 0.1, which serves as a regularizing mechanism for the model. The optimizer for training is set to ADAM with a learning rate of 0.0003, and the model was trained on each dataset for 200 epochs on a single NVIDIA Geforce RTX 3090 GPU.

	Input size	Batch size	Layers	Attention layer	Attention head	Dropout
ĺ	16×16	50	20	4	8	0.1

Table 2. PixelSnail configurations.

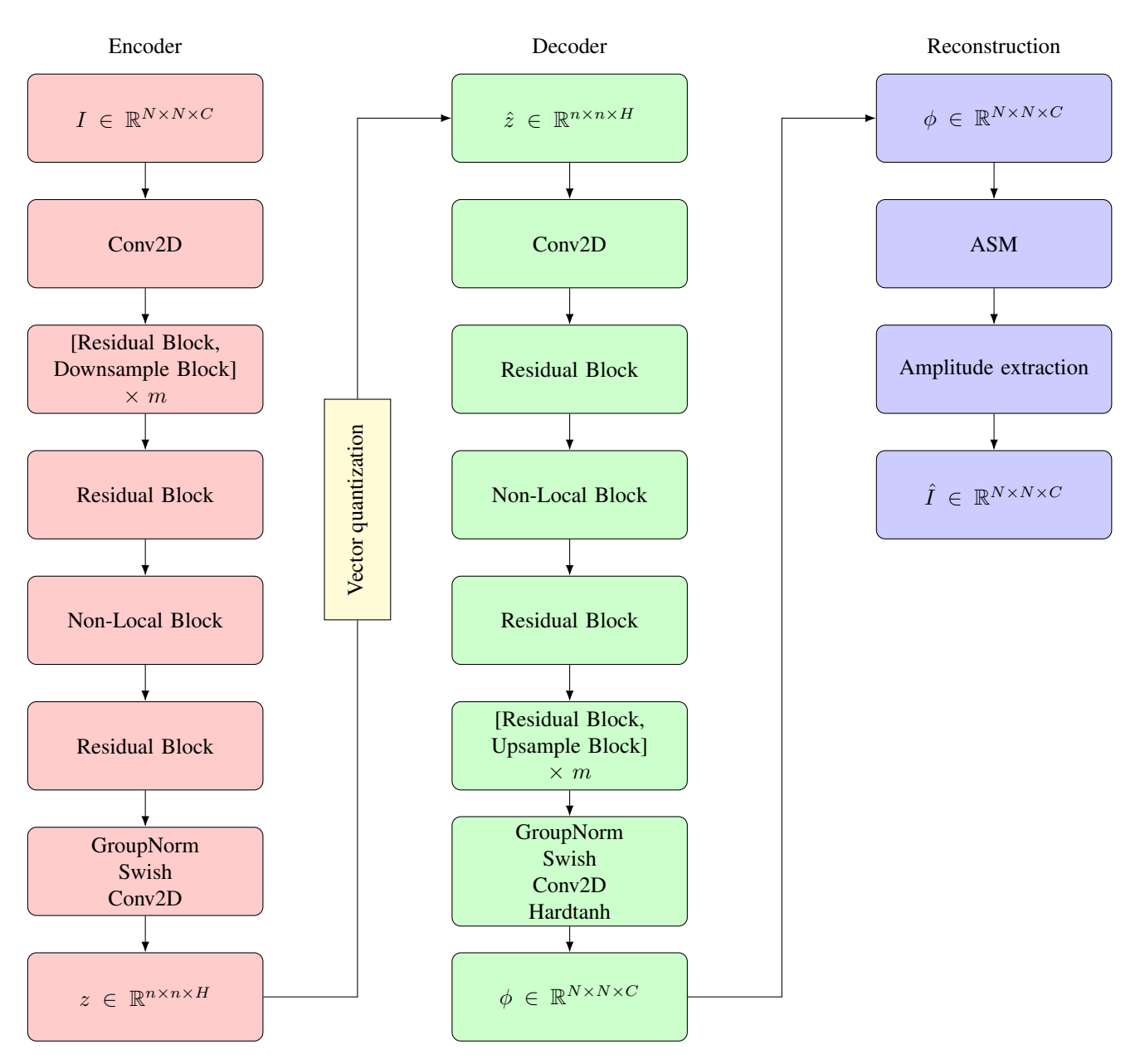


Figure 1. The pipeline of Holo-VQVAE.

2. Additional samples

This section presents additional samples of Holo-VQVAE trained on MNIST, Fashion-MNIST, and CelebA-HQ. The datasets were resized to optimize visualization and manage computational demands.

2.1. MNIST



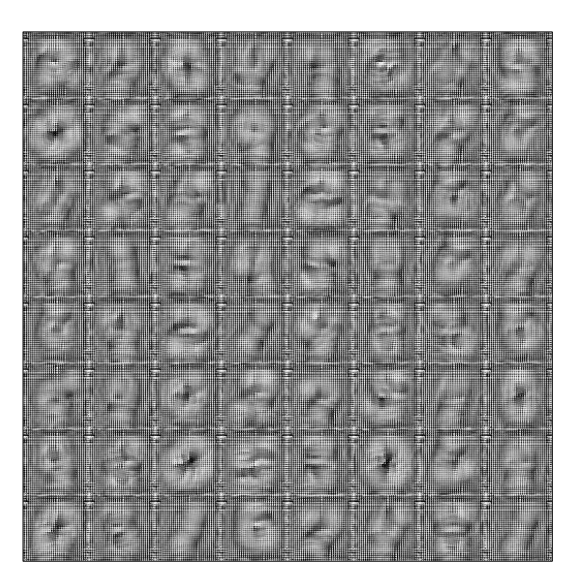


Figure 2. Representative POH samples and reconstructions of Holo-VQVAE trained on MNIST of resolution 64×64 .

2.2. Fashion-MNIST



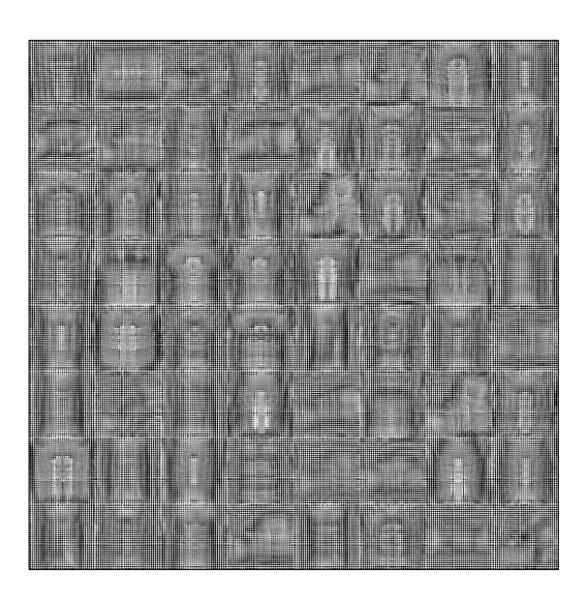


Figure 3. Representative POH samples and reconstructions of Holo-VQVAE trained on Fashion-MNIST of resolution 64×64 .

2.3. CelebA-HQ

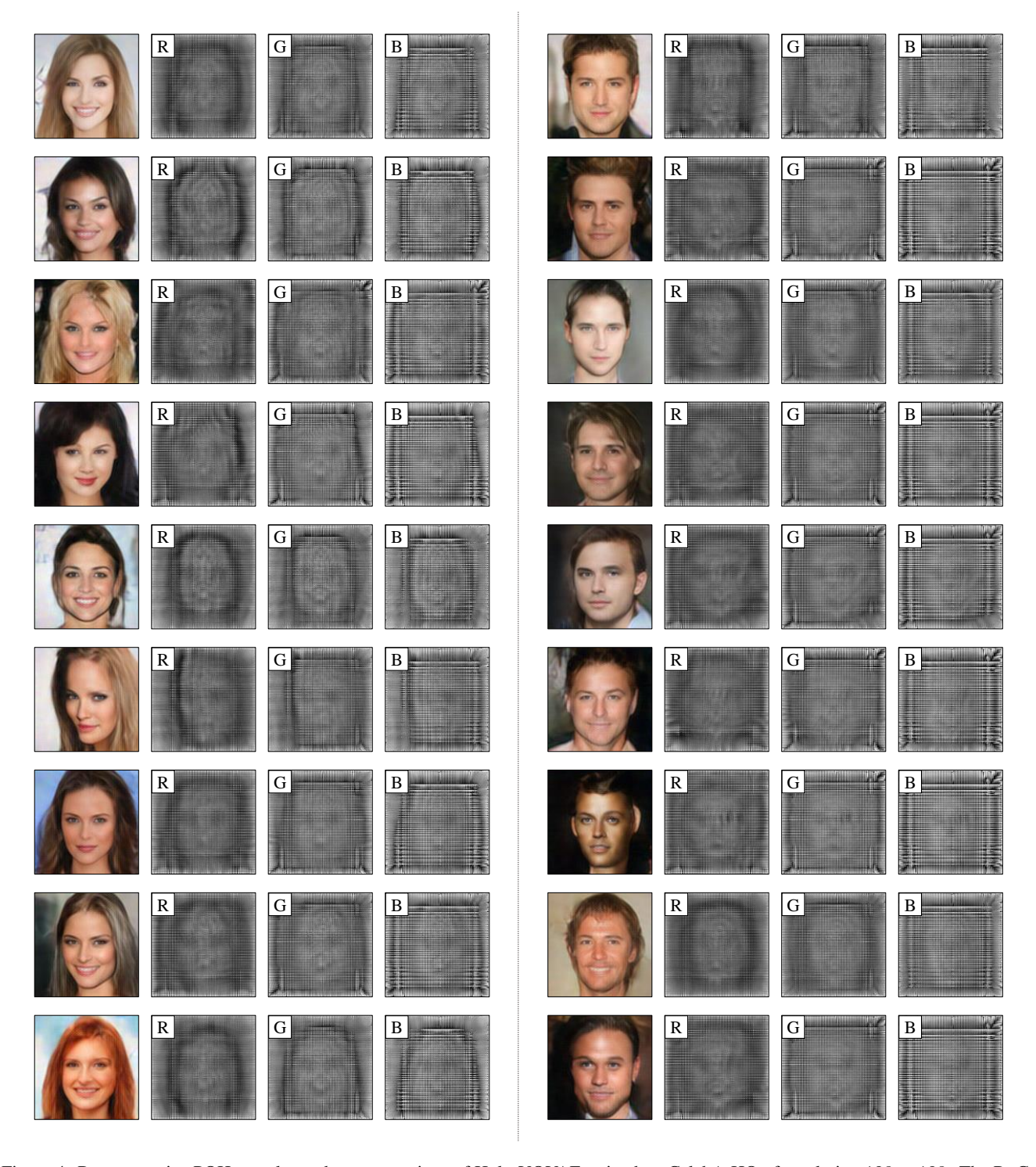


Figure 4. Representative POH samples and reconstructions of Holo-VQVAE trained on CelebA-HQ of resolution 128×128 . The R, G, and B placed on the top-left refer to the RGB channels of the sample POH, respectively.

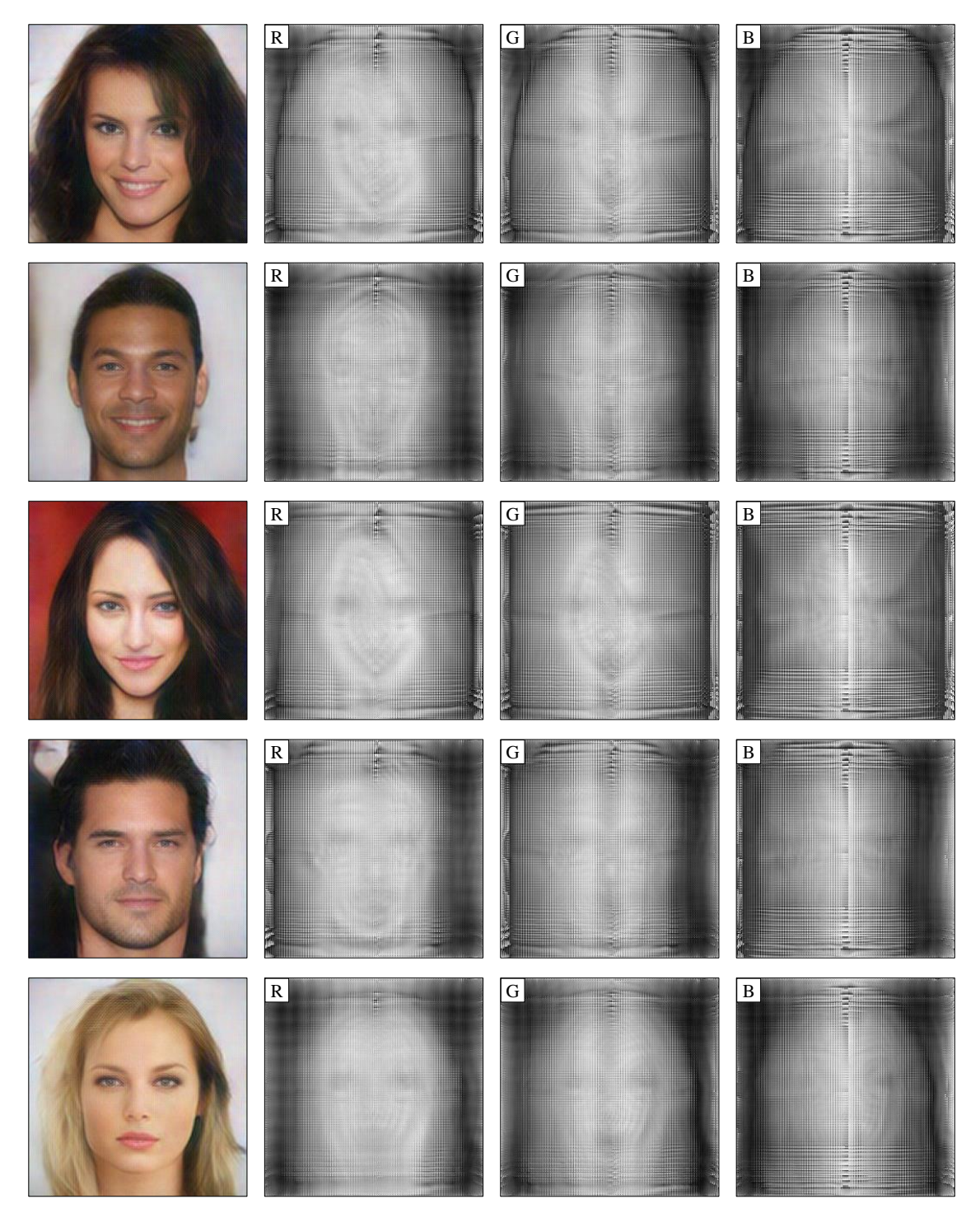


Figure 5. Representative POH samples and reconstructions of Holo-VQVAE trained on CelebA-HQ of resolution 256×256 . The R, G, and B placed on the top-left refer to the RGB channels of the sample POH, respectively.

3. Nearest neighbors of generated samples

To demonstrate the uniqueness of the generated samples, we employ the Learned Perceptual Image Patch Similarity (LPIPS) [?] metric to present training set images that show the highest similarity to the generated samples. LPIPS is a deep learning-based metric that evaluates the perceptual similarity between images by comparing the difference in high-level features extracted from a pretrained neural network. We first calculate the LPIPS scores for each training set image relative to the generated sample. Then, the top three images exhibiting the highest LPIPS scores are selected for comparison. The chosen images, also referred to as the nearest neighbors, effectively demonstrate the distinct characteristics of our generated samples.

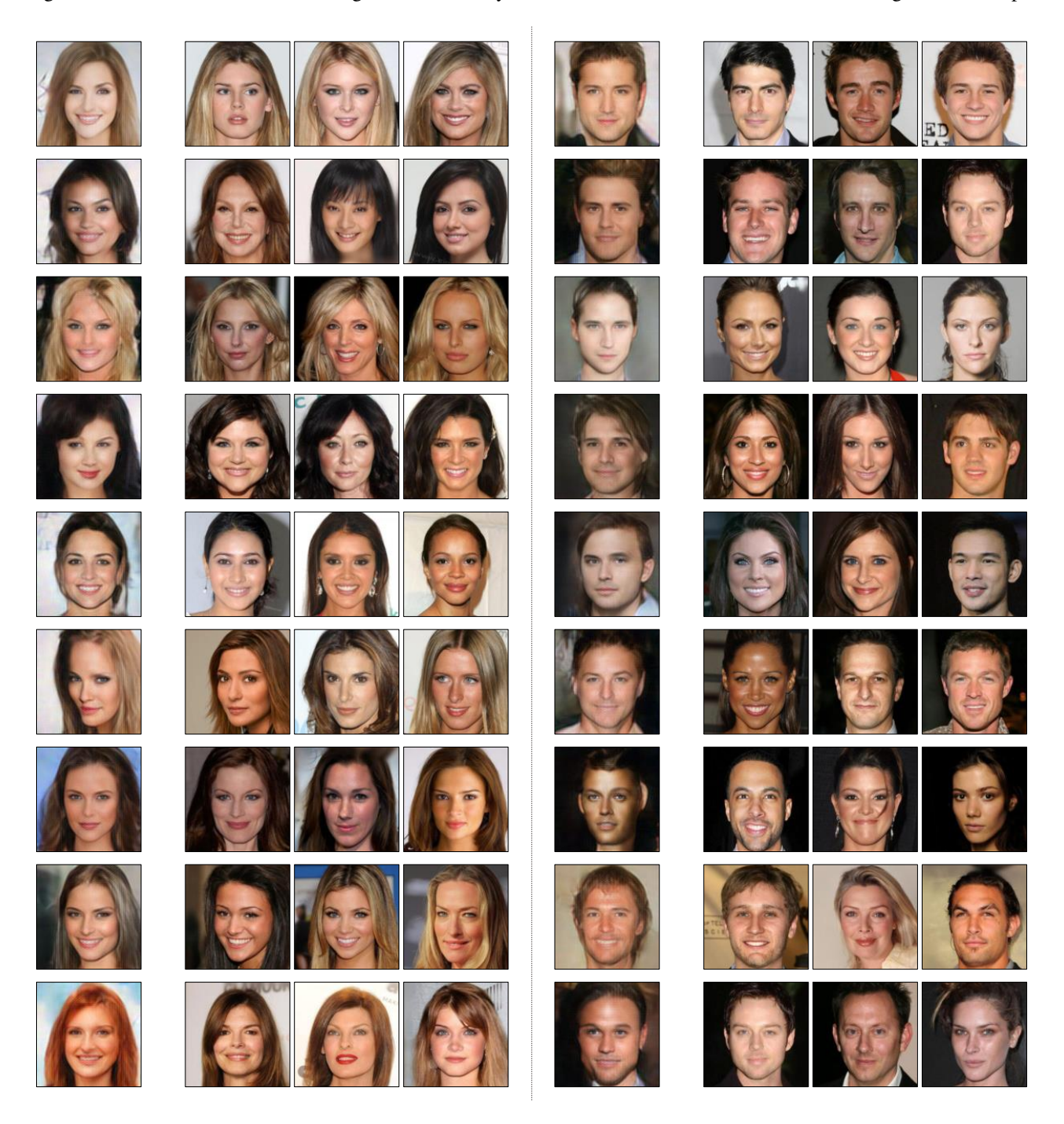


Figure 6. Representative POH sample reconstructions and top three nearest neighbors in the 128×128 CelebA-HQ training dataset.

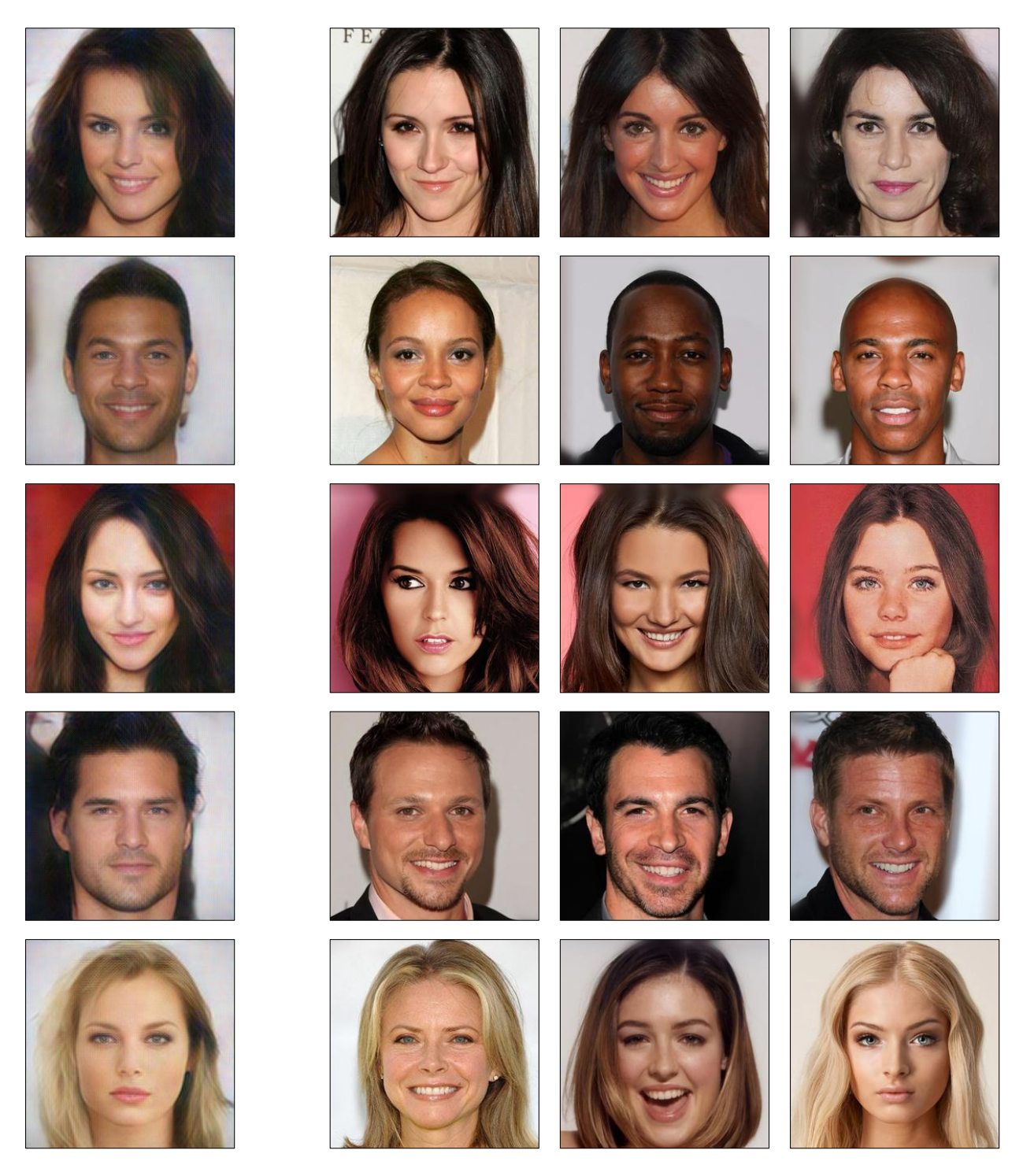


Figure 7. Representative POH sample reconstructions and top three nearest neighbors in the 256×256 CelebA-HQ training dataset.